

# Inchworm-like source evolution through a geometrically complex fault fueled persistent supershear rupture during the 2018 Palu Indonesia earthquake

Ryo Okuwaki<sup>\*,a,c</sup>, Shiro Hirano<sup>b</sup>, Yuji Yagi<sup>c</sup>, Kousuke Shimizu<sup>d</sup>

<sup>a</sup>*Mountain Science Center, University of Tsukuba, Tsukuba, Ibaraki 305-8572, Japan*

<sup>b</sup>*College of Science and Engineering, Ritsumeikan University, Kusatsu, Shiga 525-8577, Japan.*

<sup>c</sup>*Faculty of Life and Environmental Sciences, University of Tsukuba, Tsukuba, Ibaraki 305-8572, Japan*

<sup>d</sup>*Graduate School of Life and Environmental Sciences, University of Tsukuba, Tsukuba, Ibaraki 305-8572, Japan*

## Highlights

- Detailed kinematic source model was constructed for 2018 Palu earthquake
- Slip and fault geometry were simultaneously resolved by teleseismic potency-density inversion
- Transient slip acceleration and deceleration across fault bends sustained supershear rupture

## Abstract

How does fault slip follow an earthquake rupture front propagating faster than the local shear-wave velocity (i.e., at supershear speed)? How does a supershear rupture front pass through a geometrically complex fault system? Resolving the evolution of such complex earthquake ruptures is fundamental to our understanding of earthquake-source physics, but these events have not been well captured by conventional waveform inversions of observational data. We applied a new framework of finite-fault inversion to globally observed teleseismic waveforms and resolved both the spatiotemporal evolution of slip and the fault geometry of the 2018 Palu earthquake (moment magnitude 7.6) in Sulawesi, Indonesia. We show that supershear rupture propagation for this event was sustained by transient slip stagnation and advancement as the rupture front passed through the geometrically complex fault system. This peculiar inchworm-like slip evolution was caused by the rupture front encountering fault bends with favorable and unfavorable orientations for rupture propagation. Our analysis also identified the possible existence of a fault junction beneath Palu Bay connecting an unmapped primary fault in northern Sulawesi with the Palu-Koro fault in the south.

*Keywords:* 2018 Palu earthquake, Kinematic source inversion, Complex fault geometry, Supershear rupture

\*Corresponding author  
[rokuwaki@geol.tsukuba.ac.jp](mailto:rokuwaki@geol.tsukuba.ac.jp) (Ryo Okuwaki)

## 1. Introduction

How earthquake ruptures evolve within geometrically complex fault systems is an intriguing issue in earthquake science. Geometric discontinuities of fault strength or regions of increased fracture energy have been characterized as geometric barriers to rupture propagation (Das and Aki, 1977, Aki, 1979). Theoretical studies have confirmed that such barriers, which include changes of fault roughness, perturb rupture propagation (Das and Aki, 1977, Kase and Day, 2006, Huang, 2018). Seismic-waveform analyses have resolved complex evolution of ruptures associated with geometric barriers and have shown that such barriers can control both rupture direction and speed (Bouchon *et al.*, 2001, Uchide *et al.*, 2013, Okuwaki and Yagi, 2018). However, there is a need for further investigation of the relationship between the geometric complexity of a fault system and irregular high-speed rupture propagation that exceeds the local  $S$ -wave velocity (known as supershear rupture). Numerical studies have shown that although barriers disturb rupture propagation, the large stress drop as rupture propagates across the barrier can promote supershear rupture (e.g., Dunham *et al.*, 2003). Analyses of observed waveforms, however, have generated diverse views of the relationship of supershear rupture to the geometric complexity of fault systems. For example, Bouchon *et al.* (2010) reported that supershear rupture is likely promoted along smooth faults, rather than along those that are geometrically complex, and Bao *et al.* (2019) showed that supershear rupture can persist across major bends in a fault system. Nonetheless, the details of the kinematic evolution of supershear fault rupture across geometrically complex fault systems have not been well resolved from analyses of observational data.

Kinematic information about earthquake rupture can be inferred from kinematic source inversion (e.g., Olson and Apsel, 1982, Hartzell and Heaton, 1983) to resolve the spatiotemporal evolution of slip. This information is essential for understanding how slip follows an earthquake rupture front that is propagating at supershear speed and how the supershear rupture front is affected by geometric complexity, neither of which has yet been well resolved by waveform analyses. Moreover, geometric complexity in a fault system makes reliable estimation of kinematic slip evolution difficult (Shimizu *et al.*, 2020). In conventional finite-fault modeling, model fault planes are usually presumed to be either rectangular or configurations of multiple rectangles and polygons. These models may not adequately represent actual fault geometries and can increase modeling errors, thus preventing the plausible solution and robust interpretation of kinematic source processes (Mai *et al.*, 2016, Ragon *et al.*, 2018, Shimizu *et al.*, 2020). For teleseismic body waves generated by strike-slip earthquakes in particular, radiation patterns are sensitive around nodal shear planes. If such earthquakes occur in geometrically complex fault systems, radiation patterns at particular stations can vary as rupture evolves and will not be reproduced if the model fault geometry deviates from the real one.

A moment magnitude ( $M_W$ ) 7.6 2018 Palu earthquake in Sulawesi, Indonesia, satisfies such ill conditions for the finite-fault modeling; that is, strike-slip earthquake evolved along geometrically complex fault system. The southern part of its source region includes part of the Palu-Koro fault zone (Bellier *et al.*, 2001, 2006, Figs. 1 and 2), which is near the triple junction of the Australia, Eurasia (or Sunda), and

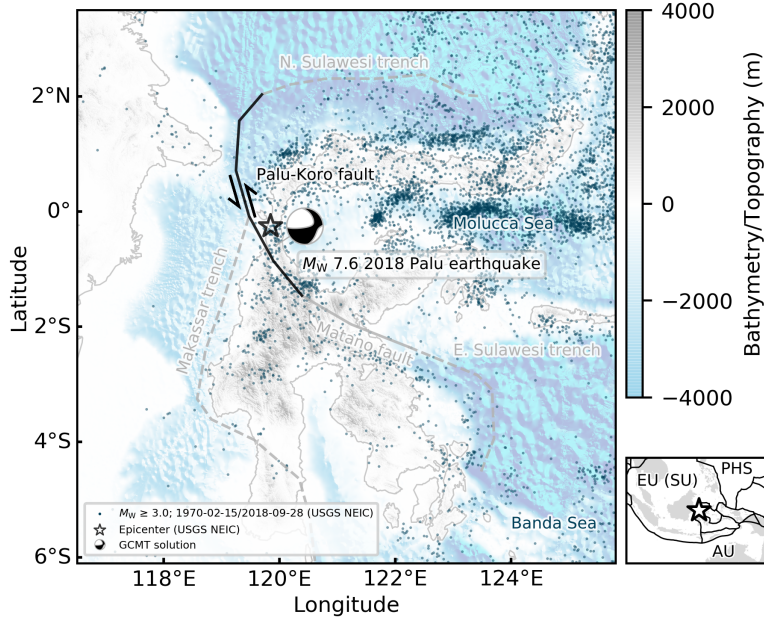


Figure 1: Overview of the study region. The background topography and bathymetry are from the GEBCO 2019 Grid (GEBCO Bathymetric Compilation Group 2019, 2019). The solid lines are the Palu-Koro and Matano faults (Bellier *et al.*, 2006). The dashed lines represent trenches (Bird, 2003). Right-bottom panel is a regional map along with names of major tectonic plates of Australia (AU), Eurasia (EU), Sunda (SU), and Philippine sea (PHS) plates. The black lines represent plate boundaries (Bird, 2003). The star denotes the epicenter.

40 Philippine sea tectonic plates (Bellier *et al.*, 2001, Socquet *et al.*, 2006). The northern part of the source  
 41 region, near the epicenter determined by the U.S. Geological Survey National Earthquake Information  
 42 Center (USGS NEIC), is on a previously unmapped north-trending fault that appears to be off-trend from  
 43 the main Palu-Koro fault zone (Fig. 2). According to the Global Centroid Moment Tensor (GCMT)  
 44 solution (GCMT; Dziewonski *et al.*, 1981, Ekström *et al.*, 2012), the 2018 Palu earthquake was the result  
 45 of left-lateral strike slip, which is consistent with pre-observed Global Positioning System velocity fields  
 46 (Bellier *et al.*, 2001, Socquet *et al.*, 2006). Interferometric Synthetic Aperture Radar (InSAR) mapping of  
 47 the surface trace of the active fault during the 2018 earthquake shows bends near the epicenter and south  
 48 of Palu Bay (Bao *et al.*, 2019, Socquet *et al.*, 2019), thus indicating that the co-seismic shear rupture  
 49 propagated along a geometrically complex fault system. Based on the spatiotemporal distribution of  
 50  $P$ -wave-radiation sources tracked by the slowness-enhanced back-projection (SEBP; Meng *et al.*, 2016),  
 51 Bao *et al.* (2019) showed that the rupture front of the 2018 Palu earthquake propagated south from the  
 52 epicenter at a sustained supershear speed ( $4.10 \pm 0.15$  km/s measured along  $174^\circ$  strike direction from  
 53 the epicenter), which was independently confirmed based on the similarity of far-field Rayleigh Mach  
 54 waves (Dunham and Bhat, 2008, Vallée and Dunham, 2012) from the mainshock of the 2018 Palu earth-  
 55 quake to those of the  $M_W$  6.1 foreshock that occurred 30 km south of the mainshock (Bao *et al.*, 2019).  
 56 Thus, the 2018 Palu earthquake is a prime candidate for using kinematic source inversion to examine  
 57 the relationship between the geometric complexity of a fault system and associated supershear rupture  
 58 propagation. Although the presence of a low-velocity damaged fault zone in the areas near the epicenter  
 59 and around Palu Bay may have been responsible for unstable rupture propagation including a supershear

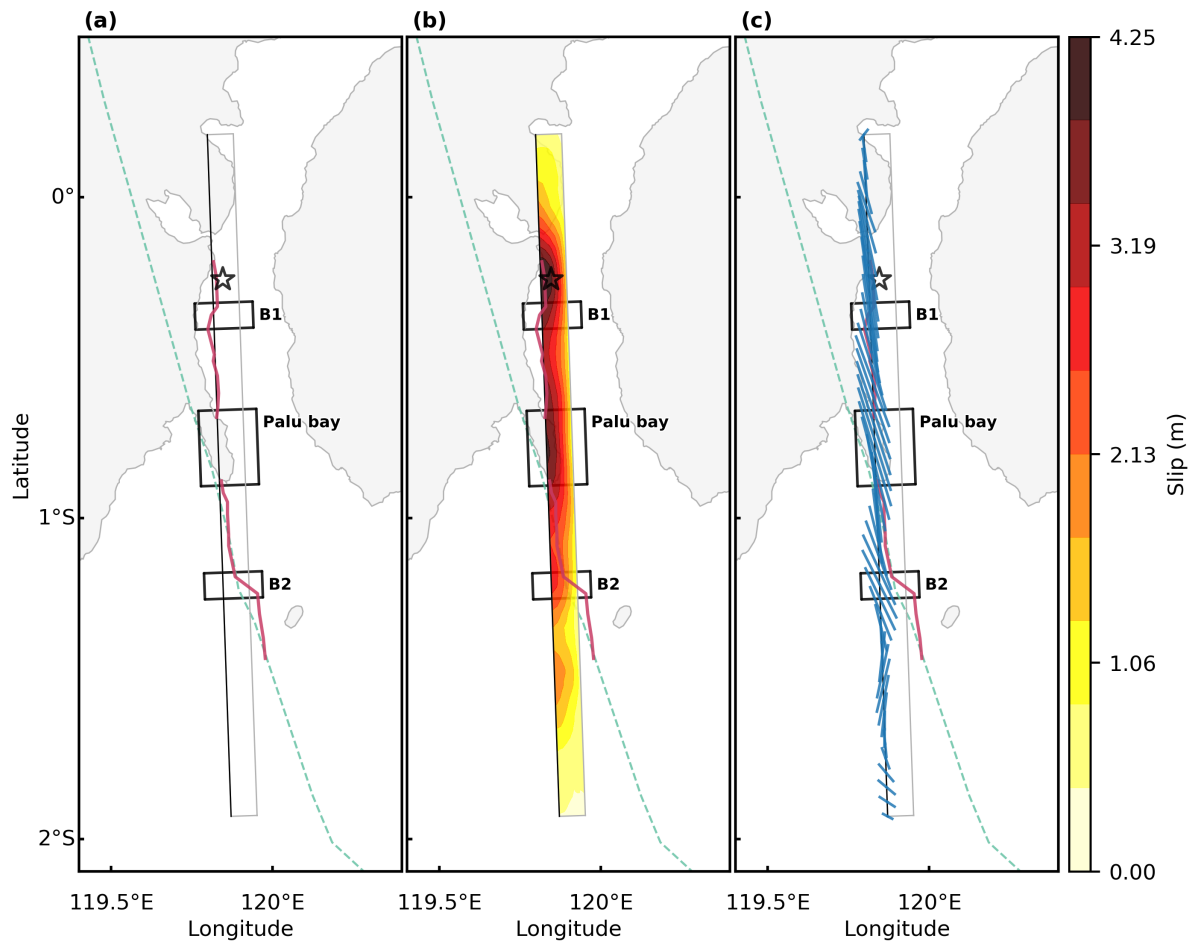


Figure 2: Result in map view. (a) Dashed line is the Palu-Koro fault (Bellier *et al.*, 2001). Red lines are the surface rupture trace mapped by the InSAR analyses (Bao *et al.*, 2019). Black rectangles shows the location of bends and Palu Bay. Gray rectangle outlines a model-fault plane and the black line is a top of the model plane. The star denotes the epicenter. (b) Color contours show the co-seismic slip resolved in this study. (c) Strike orientation extracted from the double-couple components of the resultant potency-density tensors. Only the strike distribution at the top of the model fault is shown for visual simplicity. The full set of strike distribution is shown in Fig. 3b.

60 rupture transition (Bao *et al.*, 2019, Oral *et al.*, 2020), the geometric complexity of the fault system might  
61 have been also an important control on the kinematics of the evolution of supershear rupture.

62

63 We used finite-fault inversion of globally observed teleseismic data to examine the effects of along-strike  
64 variations of fault geometry on rupture propagation and slip evolution during the 2018 Palu earthquake.  
65 We represented slip by five-basis double-couple components of potency-density tensor (Shimizu *et al.*,  
66 2020), which enabled us to represent slip along a plane that is independent from the presumed model-  
67 plane geometry. We took into account the possibility of supershear rupture by resolving slip in a wide  
68 parametric model space with a slip-rate function duration long enough and maximum rupture velocity fast  
69 enough to allow flexibility in building a slip model. Stagnation of slip behind unfavorably oriented fault  
70 bends and transient slip advancement through fault bends should provide critical observational evidence  
71 of the persistent, but transiently propagating, supershear rupture across the geometrically complex strike-  
72 slip fault.

## 73 2. Method

74 Resolving earthquake source evolution that possibly involves supershear rupture in a geometrically  
75 complex fault system requires finite-fault inversion that is more flexible than conventional inversion  
76 schemes. Conventional inverse solutions have been stabilized by limiting the model space and decreasing  
77 the degree of freedom for slip vectors. However, these limitations are not necessarily physical require-  
78 ments for representing source processes. Moreover, inappropriate assumptions about the fault geometry  
79 can increase modeling errors, produce non-unique final solutions, and make it difficult to interpret those  
80 solutions (Shimizu *et al.*, 2020, Text S1). By introducing the uncertainty of the Green’s function into  
81 the data covariance matrix (Yagi and Fukahata, 2011, Duputel *et al.*, 2014, Minson *et al.*, 2013, Ragon  
82 *et al.*, 2018), we were able to represent slip evolution without applying unnecessary solution-stabilizing  
83 constraints (e.g., non-negative slip). However still, confining a fault geometry *a priori* remains an inher-  
84 ent limitation that possibly violates the inversion solution (Shimizu *et al.*, 2020).

85

86 Complexity or spatial variations of fault geometry in a finite-fault inversion can be accounted for by  
87 representing fault deformation by fault-normal and shear-slip vectors (potency-density tensors as defined  
88 by Ampuero and Dahlen (2005)) with the five basis double-couple components (Kikuchi and Kanamori,  
89 1991). This extension of conventional source inversion makes it possible to freely represent fault-normal  
90 and shear-slip vectors on individual subfaults, whereby the fault plane spanned by slip vectors was no  
91 longer required to be identical to an arbitrarily chosen model plane geometry, thus suppressing modeling  
92 errors due to inappropriate assumptions about fault geometry (Shimizu *et al.*, 2020). As shown by our  
93 sensitivity tests (Figs. S2 and S3), a complex fault geometry represented by a mixture of focal mecha-  
94 nisms was well resolved by our inversion. For convenience, we refer here to the scalar potency density  
95 resolved by our inversion as slip. Although the units of measure for scalar potency density and slip are  
96 the same, the inverted slip we determined was underestimated because, in our inversion, we adopted a  
97 planar fault model that was not necessarily identical to the true fault, and the area of each source element

98 (subfault) of the model fault became small if the model fault deviated from the true fault. Also note  
99 that the amount of slip resolved can be underestimated owing to the smoothing constraint adopted in  
100 the inversion (Fig. S2)

101

102 Modeling of possible supershear rupture requires a vast model space to capture the high-speed rupture  
103 front and the following slip, which may endure after passage of the rupture front. In our inversion scheme,  
104 we presumed a maximum rupture speed of 5.0 km/s, which exceeded the local shear-wave velocity (Table  
105 S1), by considering the possibility of supershear rupture during the 2018 Palu earthquake on the basis of  
106 the SEBP estimates of Bao *et al.* (2019). To ensure capture of supershear rupture and the following slip  
107 within the wide model space, we allowed slip durations of 15 s at each subfault. We tested the sensitivity  
108 and robustness of our modeling for different configurations of rupture speed and slip duration (see Figs.  
109 S5–S7).

110 Then, we constructed a kinematic slip model by using the vertical component of 47 globally observed  
111 teleseismic *P* waveforms (Fig. S1). In our inversion formulation, we used five basis double-couple com-  
112 ponents of the potency-density tensor (Ampuero and Dahlen, 2005) to represent slip (Shimizu *et al.*,  
113 2020), where a priori assumptions of fault geometry for each subfault in the model space are not re-  
114 quired; instead, fault geometry is resolved by our inversion. That is, we simultaneously resolved both  
115 the spatiotemporal evolution of slip and the fault geometry of the 2018 Palu earthquake. The initial  
116 rupture point (hypocenter) was set at 0.256°S, 119.846°E, and a depth of 12.0 km, based on the origin  
117 location determined by USGS NEIC. We defined the model fault plane as a 240 km long  $\times$  30 km wide  
118 rectangle (strike 358°, dip 69°; based on the GCMT solution) discretized into evenly spaced 5 km  $\times$  5  
119 km source elements, covering the potential source region resolved by InSAR analyses (Bao *et al.*, 2019,  
120 Socquet *et al.*, 2019).

121

### 122 3. Results

123 We identified two areas of large slip on the fault: 4.25 m of slip near the epicenter and 4.0 m of slip 60  
124 km to the south (Figs. 2b and 3). The area of major slip (>50% of maximum slip) was at depths shallower  
125 than 20 km. The resultant release of seismic moment was  $0.34 \times 10^{21}$  Nm ( $M_W$  7.6), which is close to the  
126 GCMT solution of  $0.28 \times 10^{21}$  Nm ( $M_W$  7.6). The rupture front propagated mainly southward from the  
127 epicenter (Fig. 4). Areas of high slip-rate on the fault plane (closed contours defining roughly circular  
128 areas in Fig. 4 that look like eyeballs), which we refer to as “slipping patches” hereafter, were obtained  
129 near the epicenter and 60, 100, and 135 km south of the epicenter. The locus of maximum slip-rate on  
130 the fault plane within 1-s time windows, which we call the “slip-rate ridge” (Fig. 4), indicates how the  
131 slipping patches is distributed (isolated) in a certain region and time. For example, from 0 to 11 s after  
132 rupture initiation, the position along strike of the slip-rate ridge did not change, but remained close to  
133 the epicenter. From 11 to 14 s, the slip-rate ridge moved southward, indicating the southward advance  
134 of the slipping patch. Delays and advances of the slipping patch are clearly evident in snapshots of the  
135 slip-rate distribution in strike-dip view, taken at 1 s intervals from rupture initiation (Fig. 5 and Movie

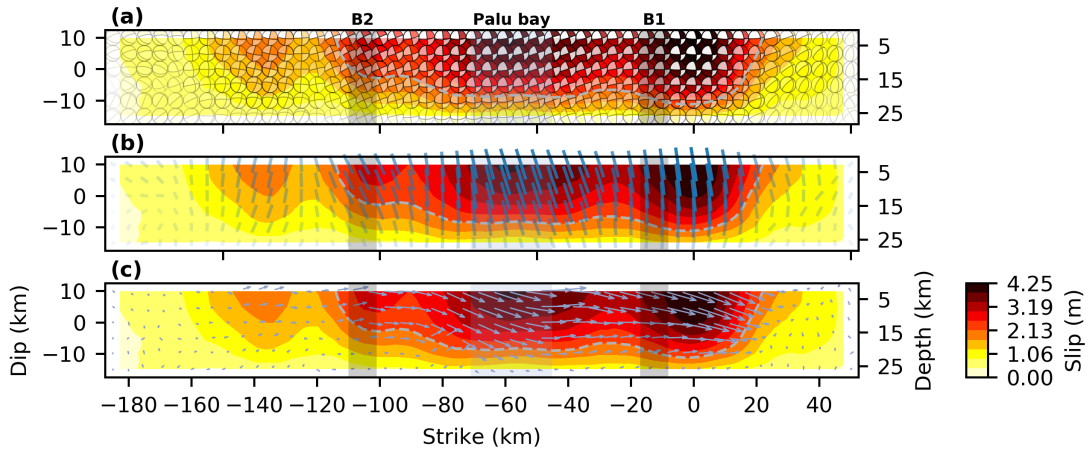


Figure 3: Static slip distribution in strike vs dip view. Background color represents the slip amplitude. Color-shaded areas are the bends and Palu Bay shown in Fig. 2. (a) The beachball shows a double-couple components of the potency-density tensor, plotted by using a lower-hemisphere stereographic projection, which are not rotated according to the model-plane geometry (not a view from side but from above). The distribution of (b) strike and (c) rake angles, which is extracted from the double-couple components of the resultant potency-density tensor. Length of line and arrow is scaled with slip.

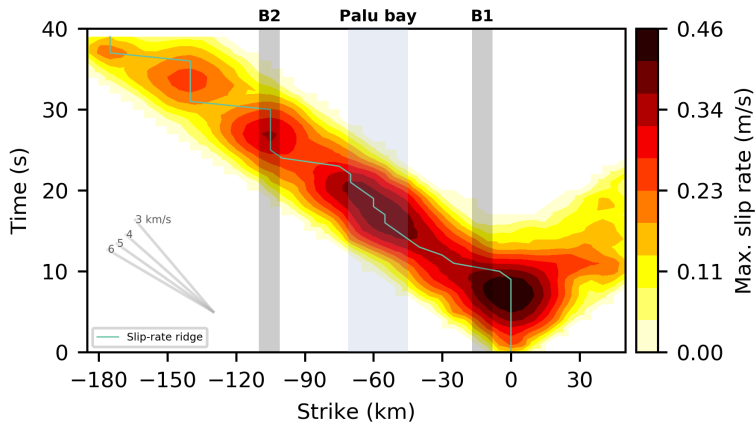


Figure 4: Temporal evolution of slip rate, projected along the model-plane strike ( $358^\circ$ ). The background color represents maximum slip-rate along dip of the model fault. The abscissa is a distance from the hypocenter, and the ordinate is a hypocentral time. The gray solid lines are the reference rupture speeds. Color-shaded areas are the bends and Palu Bay shown in Fig. 2.

136 S1). It is useful to consider three episodes of the rupture: from 8 to 17 s, 18 to 27 s, and 28 to 37 s  
137 after the initiation of rupture. In the first episode (8 to 17 s), the slipping patch remained close to the  
138 epicenter from 8 to 11 s, then moved suddenly southward from 11 to 14 s to a position 40 km south of  
139 the epicenter. In the second episode (18 to 27 s), the slipping patch remained effectively stationary from  
140 18 to 21 s, then suddenly southward from 24 to 27 s to a position 105 km south of the epicenter. The  
141 third episode (28 to 37 s) showed a similar pattern of an initial delay of the slipping patch followed by a  
142 sudden southward advance. This pattern of recurrent delay and advance of the fault slip was maintained  
143 when we changed the setting of maximum rupture velocity and slip duration (Fig. S7). Therefore, we  
144 consider them to be legitimate characteristics of the 2018 Palu earthquake.

145

146 The focal mechanism extracted from the modeled potency-density tensor showed some changes of  
147 strike orientation on subfaults relative to that of the model fault plane. The static distribution of strike  
148 orientation on subfaults for one of the nodal planes extracted from the double-couple components of the  
149 resolved potency-density tensor solution (Figs. 2c and 3b) were obtained within  $\pm 30^\circ$  of the strike of  
150 the model fault plane ( $358^\circ$ ). Deviations of the strike orientation of subfaults from that of the model  
151 fault plane were evident in the regions 30 to 70 km and 90 to 120 km south of the epicenter. Repeated  
152 rotations of the strike orientations of subfaults were also evident in snapshots of slip evolution (Figs. 5,  
153 6, and S11). When the slipping patch was near the epicenter, the strike angle was almost due north until  
154 about 10 s after rupture initiation, after which it changed to  $330^\circ$  and moved to about 30 km south of the  
155 epicenter, where rapid southward migration of the slipping patch was evident in the snapshots from 11  
156 to 14 s (Fig. 5). In snapshots from 17 to 21 s, the slipping patch was 45 to 70 km south of the epicenter  
157 and remained relatively stationary with north-northwestward strike. Snapshots from 24 to 27 s show the  
158 slipping patch migrating rapidly to about 90 km south of the epicenter with roughly northward strike,  
159 but in the snapshot at 27 s the strike had rotated again the north-northwest and maintained that strike  
160 in the region from 100 to 120 km south of the epicenter in snapshots at 28 and 31 s. Slip migration  
161 ceased about 160 km south of the epicenter with northerly strike as shown in snapshots at 34 and 37 s.  
162 The repeated rotations of strike angle seemed to correspond to alternating episodes of stagnation and  
163 advance of the slipping patch.

## 164 4. Discussion

### 165 4.1. Fault bends and supershear

166 The trace of surface rupture mapped on the basis of InSAR analyses (Bao *et al.*, 2019) shows two  
167 major bends in the Palu-Koro fault, one 10 to 25 km south of the epicenter (labeled B1 in Fig. 2) and  
168 another 100 to 110 km south of the epicenter (B2 in Fig. 2). Our finite-fault modeling showed overall  
169 persistence of supershear rupture propagation along the geometrically complex fault (Fig. 4). Dominant  
170 slipping patches were identified near the epicenter, beneath Palu Bay, and in the southern part of the  
171 fault system. The largest slip rates were modeled in the northern part of the source region from the  
172 epicenter to Palu Bay region (Figs. 4 and 5). The World Stress Map (Heidbach *et al.*, 2018) shows dif-  
173 ferent orientations of the maximum horizontal stress for the northern and southern sections of the fault,

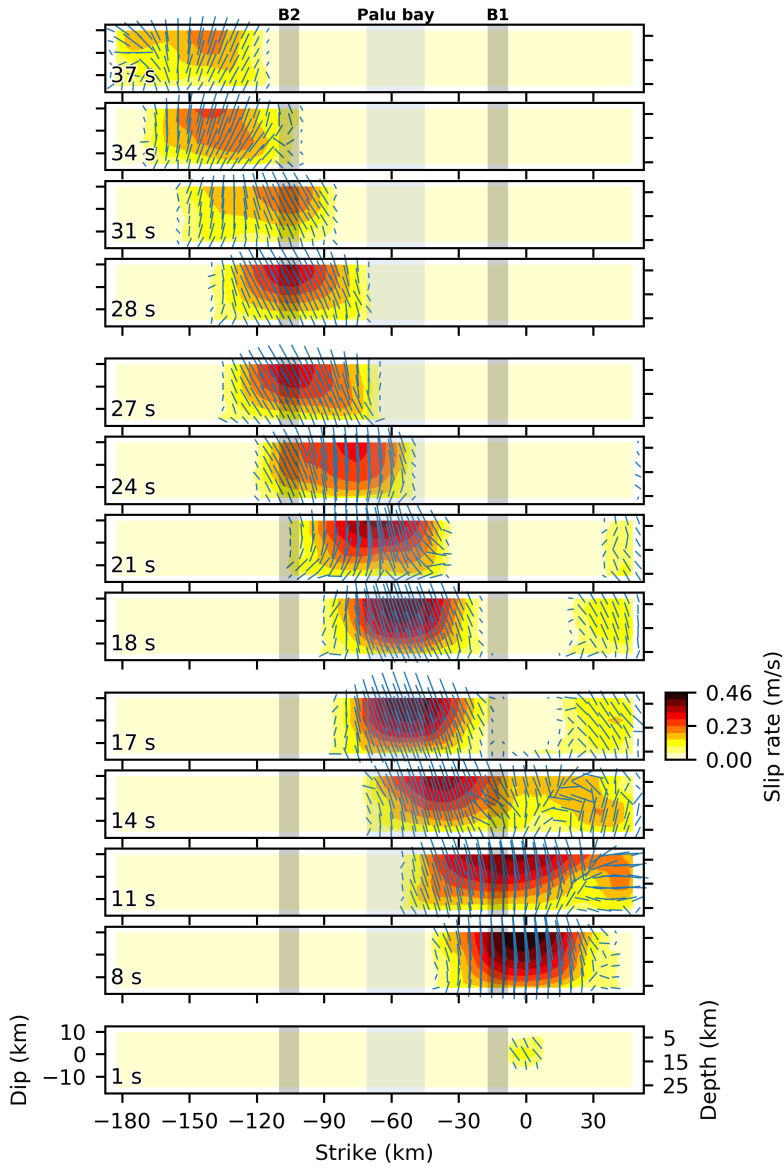


Figure 5: Snapshots of slip evolution. The background color represents slip rate. The blue line is a strike orientation. The hypocentral time at which the snapshot taken is denoted at left-bottom of each panel. Gray circles are the reference rupture speeds: 4, 5, and 6 km/s expanding from the hypocenter. Color-shaded areas are the bends and Palu Bay shown in Fig. 2.

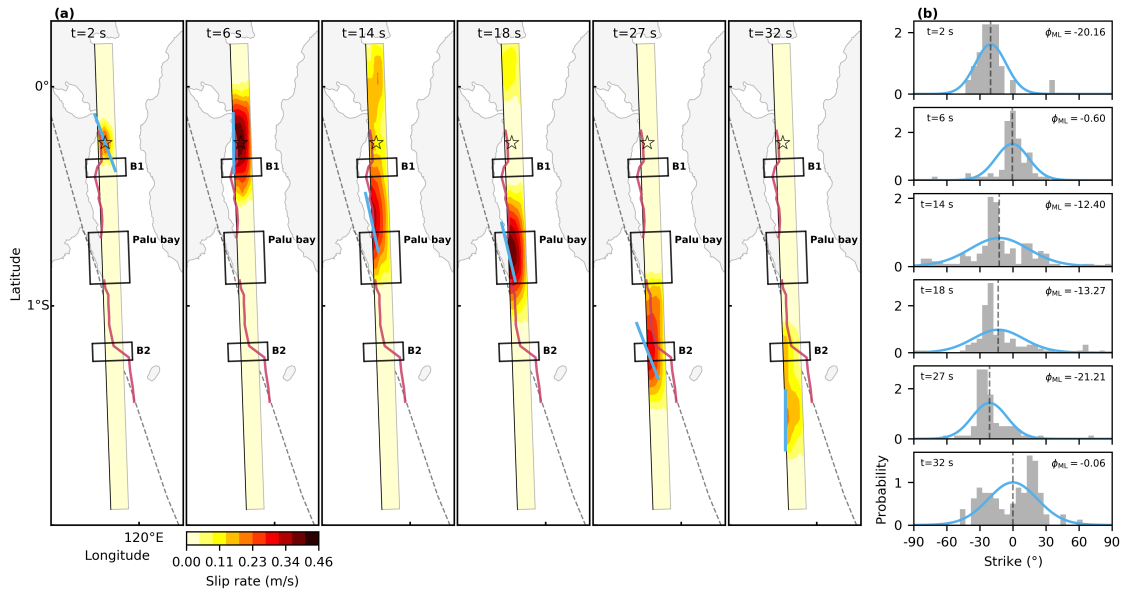


Figure 6: Selected snapshots of slip evolution and strike orientation. (a) Blue line is a maximum likelihood estimator ( $\phi_{ML}$ ) of strike orientation for the von Mises distribution (Bishop, 2006), which are estimated from set of strike orientation along the model, where we resolved slip rate  $>0$  m/s. Center of blue line corresponds to the maximum slip-rate location for each snapshot. Dashed line is the Palu-Koro fault (Bellier *et al.*, 2001). Red lines are the surface rupture traces mapped by the InSAR analyses (Bao *et al.*, 2019). Black rectangles shows the location of bends and Palu Bay. Gray rectangle outlines a model-fault plane and the black line is a top of the model plane. The star denotes the epicenter. (b) Histogram of strike orientation every  $2.5^{\circ}$  bin and its estimate of maximum likelihood. Blue curve is a probability density function for the maximum likelihood estimate of strike orientations using von Mises distribution with  $\phi_{ML}$ . All the snapshots of distribution of strike orientation and its estimate of maximum likelihood are shown in Fig. S11.

174 with the change occurring south of Palu Bay (Fig. S10). Given the known geometry of the Palu-Koro  
175 fault (Bellier *et al.*, 2001) and the fault geometry we modeled, the northern part of the fault can be  
176 considered to represent the optimal plane for maximum mean horizontal stress, which likely explains the  
177 higher slip rates we modeled there. The optimal geometry of the northern part of the fault might also  
178 explain overall persistence of supershear rupture that started early on, given the proportional relationship  
179 between peak slip-rate and rupture speed, which in a supershear regime is enhanced relative to that in a  
180 sub-shear regime (Gabriel *et al.*, 2013).

181

182 Besides the overall persistency of supershear rupture, which has been independently validated by  
183 SEBP and Mach cone analyses (Bao *et al.*, 2019), our finite-fault model resolved transient periods of  
184 stagnation and advance of the migration of the slipping patches that appear to be associated with the  
185 geometric complexity of the fault. As discussed in Results section (see also Figs. 4 and 5), during the  
186 first 10 s after rupture initiation, a dominant slipping patch with a relatively high slip rate remained in  
187 proximity to the hypocenter; then, from 11 to 17 s after rupture initiation, the slipping patch advanced  
188 rapidly southward into Palu Bay region. If we compare the location of this slipping patch with the  
189 location of the InSAR-derived surface rupture trace, it appears that there was some hesitation before  
190 the slipping patch passed through the B1 bend (Figs. 4 and 6). Given that the 2018 Palu earthquake  
191 was caused by left-lateral strike-slip faulting, and that the strike of the primary fault plane is north to  
192 north-northwest, it appears that the B1 fault bend was unfavorably oriented in relation to the optimal  
193 plane of the background stress field (Fig. S10). Bruhat *et al.* (2016) illuminated a case of supershear  
194 transition across a restraining fault bend in an area with a narrow range of background shear stress; the  
195 bend initially decelerated or arrested the rupture front, and the resultant concentration of local stress con-  
196 tributed to the subsequent acceleration of the rupture front at supershear speed when it broke through  
197 the bend. Though our kinematic source model cannot uniquely determine the dominant physical factor  
198 that controlled the rupture process, dynamic changes of normal and shear stresses across the B1 bend  
199 may have induced both the delayed migration of the slipping patch from the vicinity of the hypocenter  
200 and its subsequent advance at supershear speed.

201 Another notable bend of the 2018 Palu earthquake fault system is the B2 bend (Fig. 2), which deviates  
202 eastward from the general trend of the southern part of the Palu-Koro fault. Although the exact stress  
203 condition is difficult to be inferred, the World Stress Map (Heidbach *et al.*, 2018) shows the maximum  
204 horizontal stress is oriented at  $115\pm 11^\circ$  (Fig. S10). As demonstrated in the numerical simulation of the  
205 2018 Palu earthquake of Ulrich *et al.* (2019), favorable conditions for rupture through the B2 bend re-  
206 quire the maximum horizontal stress to be oriented east-west, which is close to the orientation according  
207 to the World Stress Map (Heidbach *et al.*, 2018). The dominant slipping patch we modeled extended  
208 to the southern edge of Palu Bay ( $\sim 70$  km south of the epicenter; Fig. 4), but then migrated rapidly  
209 southward through the B2 bend with a relatively high slip rate from 24 to 27 s after rupture initiation. It  
210 appears that the B2 bend promoted the high slip rate within an area of relatively low background stress  
211 in the southern part of the fault (Fig. S10). Numerical simulations suggested that smooth or supershear  
212 propagation along the “releasing” bend can easily occur (Trugman and Dunham, 2014, Bruhat *et al.*,

213 2016). Therefore, the B2 bend can be a releasing bend to accelerate further slip evolution toward south  
214 involving high slip-rate within the bend.

215 Thus, our results provide evidence derived from observational data that geometric complexity of a fault  
216 has a role in accelerating and decelerating rupture propagation. Although it would be difficult to deter-  
217 mine whether the accelerations and decelerations of rupture across fault bends was a result of rupture  
218 transitioning between sub-Rayleigh and supershear speeds, or perhaps a fluctuation of rupture evolution  
219 within the supershear regime, our results may provide input to further investigations of irregularities in  
220 rupture evolution associated with fault complexity in a supershear regime.

221 We note that there is a tradeoff between the locations of dominant slipping patches and the assumed  
222 maximum rupture velocity and maximum slip-rate duration for each subfault (Fig. S7); it is therefore  
223 difficult to derive a unique location of a dominant slipping patch solely from our slip models. On the basis  
224 of comparison of the locations of our dominant slipping patches with the InSAR-derived surface rupture  
225 trace, we propose that our model with a rupture velocity of 5 km/s and a slip-rate duration of 15 s  
226 provides the optimal model for the 2018 Palu earthquake, which is why we have focused on that model in  
227 the Results and Discussion sections (Figs. 2 to 6). We also identified a slipping patch at the southern end  
228 of the model fault for which slip migration ceased about 40 s after rupture initiation (Fig. 4). However,  
229 detailed evaluation of slip in this area was difficult (Text S2) because a clear surface rupture trace based  
230 on InSAR data is not available in that area, and, because of the requirement to use a rectangular model  
231 fault plane, the model fault deviates from the Palu-Koro fault line in that area (Fig. 2).

#### 232 4.2. Possible fault junction beneath Palu Bay

233 The surface rupture trace of the 2018 Palu earthquake, mapped in the northern part of the modeled  
234 region from InSAR data and reproduced by our inversion, trends approximately north, deviating from  
235 the established north-northwest trend of the Palu-Koro fault in this region (Fig. 2). South of Palu Bay,  
236 the surface rupture follows the trend of the Palu-Koro fault (Bellier *et al.*, 2001, 2006, Fig. 2), except in  
237 the area of the B2 fault bend. The change of strike between the northern and southern parts of the fault  
238 appears to be around Palu Bay. The northern part of the fault, where the 2018 rupture was initiated,  
239 had not been mapped prior to the 2018 earthquake, and if it is not part of the Palu-Koro fault system,  
240 the southward propagation rupture would need to cross a fault junction beneath Palu Bay. Although the  
241 likely fault junction is underwater and has not been identified from InSAR data, our inversion indicated  
242 that the strike of the dominant slipping patch beneath Palu Bay was north-northwest (Fig. 2c), which  
243 is consistent with that of the Palu-Koro fault. Moreover, the delayed migration of the slipping patch  
244 around Palu Bay (Fig. 4) suggests there may be a fault junction under the bay that prevents smooth  
245 slip evolution.

246 The relatively low spatial resolution of the teleseismic data we used in our inversion means that the fault  
247 geometry we resolved may not agree exactly with the surface-rupture trace mapped from InSAR analyses  
248 (Bao *et al.*, 2019, Text S2). Nonetheless, our model captured a change of strike of the fault as the rupture  
249 propagated across Palu Bay (Figs. 2 and 5).

250 Another notable feature identified by our inversion beneath Palu Bay is that the focal mechanism we de-

251 terminated there indicates normal dip-slip. We therefore suggest the dominant slipping patch beneath Palu  
252 Bay may have contributed to generation of the 2018 Palu tsunami, which is consistent with earthquake-  
253 tsunami modeling by Ulrich *et al.* (2019).

#### 254 4.3. *Inchworm-like slip evolution; How do we infer rupture behavior from inversion?*

255 In our inversion scheme, the relationship between slip migration and rupture-front propagation is non-  
256 trivial because we explicitly assumed a maximum rupture velocity; therefore, the rupture front (the edge  
257 of the model space where the following slip is represented) is arbitrarily defined by that velocity. We now  
258 consider a simple kinematic slip model (Fig. S9 and Text S4) in which we assume that a rupture pulse  
259 propagates at constant rupture-front velocity with oscillating slip velocity. This simple kinematic model,  
260 involving only the oscillation of slip velocity, can be realized if there is a heterogeneous distribution of  
261 breakdown stress drop, even if the rupture front propagates at a constant speed, given that maximum  
262 slip velocity is proportional to breakdown stress drop (Ida, 1972, Gabriel *et al.*, 2012). The pattern of the  
263 slip-rate distribution obtained for this model (Fig. S9) looks similar to that we obtained in our inversion  
264 (Fig. 4). However, the slip-rate ridge in this simple kinematic model is a straight line, indicating that the  
265 location of the slipping patch is migrating at constant speed, even though the slip velocity is oscillating. In  
266 our slip model for the 2018 Palu earthquake (Fig. 4), the slip-rate ridge shows a zigzag pattern involving  
267 periods of stangancy and advancement of slip, which is not explained by the above simple kinematic  
268 model. In our inversion, we resolved changes of rupture velocity followed by peculiar repetitions of slip  
269 deceleration and acceleration associated with fault bends in the geometrically complex fault system; we  
270 called this inchworm-like slip evolution. The modeled migration speed of the slipping patch is well above  
271 the local  $S$ -wave velocity ( $>4$  km/s; Figs. 4 and 5; Text S3), both when it advanced across the B1  
272 fault bend and when it passed through the B2 fault bend after traversing the possible fault junction  
273 beneath Palu Bay. If we assume that the migration of the slipping patch follows the rupture front, our  
274 inversion result should represent supershear rupture evolution related to the geometric complexity of the  
275 fault system. Thus, we propose that the geometric complexity of a fault system can be a key factor in  
276 promoting persistent supershear rupture, which enhanced by recurrent inchworm-like slip evolution (Fig.  
277 6 and Movie S1).

## 278 Conclusion

279 Our modeling of slip during the 2018 Palu earthquake showed a peculiar evolution of slip that man-  
280 ifested as repetitive periods of stagnation and advancement of slip that appeared to be associated with  
281 two fault bends and a possible fault junction beneath Palu Bay. We propose that the overall persistence  
282 of supershear rupture propagation during the 2018 Palu earthquake was a response to the geometric  
283 complexity of the fault system, which was the key driver of the transient and episodic acceleration and  
284 deceleration of slip evolution.

## 285 Acknowledgements

286 We thank the editor and the reviewers for their handling and thorough review of this manuscript.  
287 This work was supported by Grants-in-Aid for Japan Society for the Promotion of Science (JSPS) Fellows  
288 (JP16J00298 and JP19J00814) and a Grant-in-Aid for Scientific Research (JP19K04030). The authors  
289 thank Han Bao and Jean-Paul Ampuero for providing the surface rupture trace and the results of their  
290 SEBP analyses of the 2018 Palu earthquake (Bao *et al.*, 2019) and for their helpful comments on our  
291 work. Teleseismic waveforms were obtained from the following networks: the Australian National Seis-  
292 mograph Network (AU), GEOSCOPE (G; <https://doi.org/10.18715/GEOSCOPE.G>); the New China  
293 Digital Seismograph Network (IC; <https://doi.org/10.7914/SN/IC>); the Global Seismograph Network  
294 (GSN IRIS/IDA, II; <https://doi.org/10.7914/SN/II>), and the Global Seismograph Network (GSN  
295 IRIS/USGS, IU; <https://doi.org/10.7914/SN/IU>). All teleseismic waveform data were downloaded  
296 through the IRIS-DMC (<https://ds.iris.edu/ds/nodes/dmc/>). The topography and bathymetry  
297 used in Fig. 1 are from GEBCO 2019 Grid (GEBCO Bathymetric Compilation Group 2019, 2019,  
298 <https://doi.org/10/c33m>). The figures were generated with matplotlib (Hunter, 2007, Version v3.0.0;  
299 <https://doi.org/10.5281/zenodo.1420605>) and ObsPy (Beyreuther *et al.*, 2010, Megies *et al.*, 2011,  
300 Krischer *et al.*, 2015, Version v1.1.0; <https://doi.org/10.5281/zenodo.599698>). All the data and  
301 results presented in this study are stored in a Github repository (<https://github.com/rokuwaki>).

## 302 References

- 303 Aki, K., 1979. Characterization of barriers on an earthquake fault, *J. Geophys. Res.*, **84**(B11), 6140, doi:  
304 [10.1029/JB084iB11p06140](https://doi.org/10.1029/JB084iB11p06140).
- 305 Ampuero, J.-P. and Dahlen, F. A., 2005. Ambiguity of the Moment Tensor, *Bull. Seism. Soc. Am.*, **95**(2), 390, doi:  
306 [10.1785/0120040103](https://doi.org/10.1785/0120040103).
- 307 Bao, H., Ampuero, J.-P., Meng, L., Fielding, E. J., Liang, C., Milliner, C. W. D., Feng, T., and Huang, H., 2019.  
308 Early and persistent supershear rupture of the 2018 magnitude 7.5 Palu earthquake, *Nat. Geosci.*, **12**(3), 200–205,  
309 doi: [10.1038/s41561-018-0297-z](https://doi.org/10.1038/s41561-018-0297-z).
- 310 Bellier, O., Sebrier, M., Beaudouin, T., Villeneuve, M., Braucher, R., Bourles, D., Siame, L., Putranto, E., and Pratomo,  
311 I., 2001. High slip rate for a low seismicity along the Palu-Koro active fault in central Sulawesi (Indonesia), *Terra Nov.*,  
312 **13**(6), 463–470, doi: [10.1046/j.1365-3121.2001.00382.x](https://doi.org/10.1046/j.1365-3121.2001.00382.x).
- 313 Bellier, O., Sébrier, M., Seward, D., Beaudouin, T., Villeneuve, M., and Putranto, E., 2006. Fission track and fault  
314 kinematics analyses for new insight into the Late Cenozoic tectonic regime changes in West-Central Sulawesi (Indonesia),  
315 *Tectonophysics*, **413**(3-4), 201–220, doi: [10.1016/j.tecto.2005.10.036](https://doi.org/10.1016/j.tecto.2005.10.036).
- 316 Beyreuther, M., Barsch, R., Krischer, L., Megies, T., Behr, Y., and Wassermann, J., 2010. ObsPy: A Python Toolbox for  
317 Seismology, *Seismol. Res. Lett.*, **81**(3), 530–533, doi: [10.1785/gssrl.81.3.530](https://doi.org/10.1785/gssrl.81.3.530).
- 318 Bird, P., 2003. An updated digital model of plate boundaries, *Geochemistry, Geophys. Geosystems*, **4**(3), 1105, doi:  
319 [10.1029/2001GC000252](https://doi.org/10.1029/2001GC000252).
- 320 Bishop, C. M., 2006. *Pattern Recognition and Machine Learning*, Springer.
- 321 Bouchon, M., Bouin, M.-P., Karabulut, H., Toksöz, M. N., Dietrich, M., and Rosakis, A. J., 2001. How fast is rupture  
322 during an earthquake? New insights from the 1999 Turkey Earthquakes, *Geophys. Res. Lett.*, **28**(14), 2723–2726, doi:  
323 [10.1029/2001GL013112](https://doi.org/10.1029/2001GL013112).
- 324 Bouchon, M., Karabulut, H., Bouin, M.-P., Schmittbuhl, J., Vallée, M., Archuleta, R., Das, S., Renard, F., and  
325 Marsan, D., 2010. Faulting characteristics of supershear earthquakes, *Tectonophysics*, **493**(3-4), 244–253, doi:  
326 [10.1016/j.tecto.2010.06.011](https://doi.org/10.1016/j.tecto.2010.06.011).

327 Bruhat, L., Fang, Z., and Dunham, E. M., 2016. Rupture complexity and the supershear transition on rough faults, *J.*  
328 *Geophys. Res. Solid Earth*, **121**(1), 210–224, doi: 10.1002/2015JB012512.

329 Das, S. and Aki, K., 1977. Fault plane with barriers: A versatile earthquake model, *J. Geophys. Res.*, **82**(36), 5658–5670,  
330 doi: 10.1029/JB082i036p05658.

331 Dunham, E. M. and Bhat, H. S., 2008. Attenuation of radiated ground motion and stresses from three-dimensional  
332 supershear ruptures, *J. Geophys. Res. Solid Earth*, **113**(B8), 1–17, doi: 10.1029/2007JB005182.

333 Dunham, E. M., Favreau, P., and Carlson, J. M., 2003. A supershear transition mechanism for cracks, *Science (80-. )*,  
334 **299**(5612), 1557–1559, doi: 10.1126/science.1080650.

335 Duputel, Z., Agram, P. S., Simons, M., Minson, S. E., and Beck, J. L., 2014. Accounting for prediction uncertainty when  
336 inferring subsurface fault slip, *Geophys. J. Int.*, **197**(1), 464–482, doi: 10.1093/gji/ggt517.

337 Dziewonski, A. M., Chou, T.-A., and Woodhouse, J. H., 1981. Determination of earthquake source parameters from  
338 waveform data for studies of global and regional seismicity, *J. Geophys. Res. Solid Earth*, **86**(B4), 2825–2852, doi:  
339 10.1029/JB086iB04p02825.

340 Ekström, G., Nettles, M., and Dziewoński, A., 2012. The global CMT project 2004–2010: Centroid-moment tensors for  
341 13,017 earthquakes, *Phys. Earth Planet. Inter.*, **200–201**, 1–9, doi: 10.1016/j.pepi.2012.04.002.

342 Gabriel, A.-A., Ampuero, J.-P., Dalguer, L. A., and Mai, P. M., 2012. The transition of dynamic rupture styles in elastic  
343 media under velocity-weakening friction, *J. Geophys. Res. Solid Earth*, **117**(B9), 1–20, doi: 10.1029/2012JB009468.

344 Gabriel, A.-A., Ampuero, J.-P., Dalguer, L. A., and Mai, P. M., 2013. Source properties of dynamic rupture pulses with  
345 off-fault plasticity, *J. Geophys. Res. Solid Earth*, **118**(8), 4117–4126, doi: 10.1002/jgrb.50213.

346 GEBCO Bathymetric Compilation Group 2019, 2019. The GEBCO\_2019 Grid - a continuous terrain model of the global  
347 oceans and land, doi: <https://doi.org/10/c33m>.

348 Hartzell, S. H. and Heaton, T. H., 1983. Inversion of strong ground motion and teleseismic waveform data for the fault  
349 rupture history of the 1979 Imperial Valley, California, earthquake, *Bull. Seism. Soc. Am.*, **73**(6A), 1553.

350 Heidbach, O., Rajabi, M., Cui, X., Fuchs, K., Müller, B., Reinecker, J., Reiter, K., Tingay, M., Wenzel, F., Xie, F., Ziegler,  
351 M. O., Zoback, M.-L., and Zoback, M., 2018. The World Stress Map database release 2016: Crustal stress pattern across  
352 scales, *Tectonophysics*, **744**, 484–498, doi: 10.1016/j.tecto.2018.07.007.

353 Huang, Y., 2018. Earthquake Rupture in Fault Zones With Along-Strike Material Heterogeneity, *J. Geophys. Res. Solid*  
354 *Earth*, **123**(11), 9884–9898, doi: 10.1029/2018JB016354.

355 Hunter, J. D., 2007. Matplotlib: A 2D Graphics Environment, *Comput. Sci. Eng.*, **9**(3), 90–95, doi: 10.1109/MCSE.2007.55.

356 Ida, Y., 1972. Cohesive force across the tip of a longitudinal-shear crack and Griffith’s specific surface energy, *J. Geophys.*  
357 *Res.*, **77**(20), 3796–3805, doi: 10.1029/JB077i020p03796.

358 Kase, Y. and Day, S. M., 2006. Spontaneous rupture processes on a bending fault, *Geophys. Res. Lett.*, **33**(10), 1–4, doi:  
359 10.1029/2006GL025870.

360 Kikuchi, M. and Kanamori, H., 1991. Inversion of complex body waves-III, *Bull. Seism. Soc. Am.*, **81**(6), 2335–2350.

361 Krischer, L., Megies, T., Barsch, R., Beyreuther, M., Lecocq, T., Caudron, C., and Wassermann, J., 2015. ObsPy: a  
362 bridge for seismology into the scientific Python ecosystem, *Comput. Sci. Discov.*, **8**(1), 014003, doi: 10.1088/1749-  
363 4699/8/1/014003.

364 Mai, P. M., Schorlemmer, D., Page, M., Ampuero, J., Asano, K., Causse, M., Custodio, S., Fan, W., Festa, G., Galis, M.,  
365 Gallovic, F., Imperatori, W., Käser, M., Malytsky, D., Okuwaki, R., Pollitz, F., Passone, L., Razafindrakoto, H. N. T.,  
366 Sekiguchi, H., Song, S. G., Somala, S. N., Thingbaijam, K. K. S., Twardzik, C., van Driel, M., Vyas, J. C., Wang, R.,  
367 Yagi, Y., and Zielke, O., 2016. The Earthquake-Source Inversion Validation (SIV) Project, *Seismol. Res. Lett.*, **87**(3),  
368 690–708, doi: 10.1785/0220150231.

369 Megies, T., Beyreuther, M., Barsch, R., Krischer, L., and Wassermann, J., 2011. ObsPy – What can it do for data centers  
370 and observatories?, *Ann. Geophys.*, **54**(1), 47–58, doi: 10.4401/ag-4838.

371 Meng, L., Zhang, A., and Yagi, Y., 2016. Improving back projection imaging with a novel physics-based after-  
372 shock calibration approach: A case study of the 2015 Gorkha earthquake, *Geophys. Res. Lett.*, **43**(2), 628–636, doi:  
373 10.1002/2015GL067034.

374 Minson, S. E., Simons, M., and Beck, J. L., 2013. Bayesian inversion for finite fault earthquake source models I-theory and  
375 algorithm, *Geophys. J. Int.*, **194**(3), 1701–1726, doi: 10.1093/gji/ggt180.

376 Okuwaki, R. and Yagi, Y., 2018. Role of geometric barriers in irregular-rupture evolution during the 2008 Wenchuan  
377 earthquake, *Geophys. J. Int.*, **212**(3), 1657–1664, doi: 10.1093/gji/ggx502.

378 Olson, A. H. and Apsel, R. J., 1982. Finite faults and inverse theory with applications to the 1979 Imperial Valley earthquake,  
379 *Bull. Seism. Soc. Am.*, **72**(6A), 1969.

380 Oral, E., Weng, H., and Ampuero, J. P., 2020. Does a damaged-fault zone mitigate the near-field impact of supershear earth-  
381 quakes?—Application to the 2018 M w 7.5 Palu, Indonesia earthquake, *Geophys. Res. Lett.*, doi: 10.1029/2019GL085649.

382 Ragon, T., Sladen, A., and Simons, M., 2018. Accounting for uncertain fault geometry in earthquake source inversions – I:  
383 theory and simplified application, *Geophys. J. Int.*, **214**(2), 1174–1190, doi: 10.1093/gji/ggy187.

384 Shimizu, K., Yagi, Y., Okuwaki, R., and Fukahata, Y., 2020. Development of an inversion method to extract information  
385 on fault geometry from teleseismic data, *Geophys. J. Int.*, **220**(2), 1055–1065, doi: 10.1093/gji/ggz496.

386 Socquet, A., Simons, W., Vigny, C., McCaffrey, R., Subarya, C., Sarsito, D., Ambrosius, B., and Spakman, W., 2006.  
387 Microblock rotations and fault coupling in SE Asia triple junction (Sulawesi, Indonesia) from GPS and earthquake slip  
388 vector data, *J. Geophys. Res.*, **111**(B8), B08409, doi: 10.1029/2005JB003963.

389 Socquet, A., Hollingsworth, J., Pathier, E., and Bouchon, M., 2019. Evidence of supershear during the 2018 magnitude 7.5  
390 Palu earthquake from space geodesy, *Nat. Geosci.*, **12**(3), 192–199, doi: 10.1038/s41561-018-0296-0.

391 Trugman, D. T. and Dunham, E. M., 2014. A 2D Pseudodynamic Rupture Model Generator for Earthquakes on Geomet-  
392 rically Complex Faults, *Bull. Seismol. Soc. Am.*, **104**(1), 95–112, doi: 10.1785/0120130138.

393 Uchide, T., Yao, H., and Shearer, P. M., 2013. Spatio-temporal distribution of fault slip and high-frequency radiation of the  
394 2010 El Mayor-Cucapah, Mexico earthquake, *J. Geophys. Res. Solid Earth*, **118**(4), 1546–1555, doi: 10.1002/jgrb.50144.

395 Ulrich, T., Vater, S., Madden, E. H., Behrens, J., van Dinther, Y., van Zelst, I., Fielding, E. J., Liang, C., and Gabriel,  
396 A., 2019. Coupled, Physics-Based Modeling Reveals Earthquake Displacements are Critical to the 2018 Palu, Sulawesi  
397 Tsunami, *Pure Appl. Geophys.*, **176**(10), 4069–4109, doi: 10.1007/s00024-019-02290-5.

398 Vallée, M. and Dunham, E. M., 2012. Observation of far-field Mach waves generated by the 2001 Kokoxili supershear  
399 earthquake, *Geophys. Res. Lett.*, **39**(5), 1–5, doi: 10.1029/2011GL050725.

400 Yagi, Y. and Fukahata, Y., 2011. Introduction of uncertainty of Green’s function into waveform inversion for seismic source  
401 processes, *Geophys. J. Int.*, **186**(2), 711–720, doi: 10.1111/j.1365-246X.2011.05043.x.